# Rarefied gas flow through short tubes into vacuum

S. Varoutis and D. Valougeorgis[a)]
*Department of Mechanical and Industrial Engineering, University of Thessaly, Pedion Areos, Volos 38334, Greece*

O. Sazhin
*Department of Physics, Ural State University, Yekaterinburg 620083, Russia*

F. Sharipov
*Departamento de Física, Universidade Federal do Paraná, Caixa Postal 19044, Curitiba 81531-990, Brazil*

(Received 26 October 2007; accepted 6 December 2007; published 24 January 2008)

A rarefied gas flow into vacuum through a tube of finite length is investigated over the whole range of gas rarefaction by the direct simulation Monte Carlo method. The nonequilibrium effects at the inlet and outlet of the tube have been considered by including in the computational domain large volumes of the upstream and downstream reservoirs. Results for the dimensionless flow rate and for the flow field are presented for a wide range of the gas rarefaction and for various values of the length to radius ratio in the range from 0 to 10. The influence of the gas-surface interaction model, as well as the effect of the intermolecular potential model on the gas flow, is examined. A good agreement has been obtained between the present numerical results and the corresponding experimental ones available in the literature. © *2008 American Vacuum Society.*
[DOI: 10.1116/1.2830639]

## I. INTRODUCTION

Rarefied gas flows through pipes of finite length have been extensively investigated over the past years both numerically and experimentally. The characteristics of such flows are viable in the design of several industrial applications including vacuum pumping systems, equipment and devices for space applications, filtration through porous media and membranes, and fabrication of semiconductors and microelectronics. In all these applications, the operation of the system may be under low, medium, or high vacuum conditions. In several occasions, the characteristic dimension of the system may be of the same order or even larger than the mean free path of the gas. Therefore, the flow may occur over the whole range of the Knudsen number.

A detailed and comprehensive summary of published works related to gas flows through capillaries of finite length can be found in Sec. V of the review article by Sharipov and Seleznev.[1] It is well known that the simulation of flows through short tubes compared to those for infinitely long tubes contains certain difficulties. In the latter case, even for large pressures differences, the flow is linear (fully developed) and linearized kinetic theory[2] has been applied with considerable success.[3–7] In the former case, usually, the flow is strongly nonequilibrium and has to be tackled by nonlinear kinetic equations[2] or alternatively by the direct simulation Monte Carlo (DSMC) method.[8] Moreover, when the flow is in the transition and continuum regimes, the distribution functions at the entrance and the exit of the capillary are not Maxwellians and therefore the computational domain in both approaches (nonlinear kinetic equations and DSMC) must include the containers before and after the capillary. Consequently, the computational effort for solving flows through tubes of finite length is significantly increased compared to the one required for tubes of infinite length. Despite all these difficulties, as it is pointed in Ref. 1, there have been several significant contributions in the simulation of rarefied gas flows through short tubes, while more recent work on this topic may be found in Refs. 9–11. It is evident, however, that additional research work is needed in order to provide a more complete data frame for a wide range of geometric and flow parameters as well as the dependency of the flow characteristics on various gas-surface interaction models and intermolecular potentials.

In that framework, Shinagawa *et al.*[9] extended earlier work by Usami and Teshima,[12] to compute and measure the conductance of nitrogen gas through circular tubes of various length to diameter ratios and for several pressure ratios across the tube. Both experimental and computational conductances were found to be lower than the ones provided by the Hanks-Weissberg equation.[13] Very recently, Lilly *et al.*,[11] in an effort to optimize the design of short tubes for aerospace propulsion, have studied in detail the effect of the length of thin wall orifices. They have examined tubes with two length to diameter ratios, namely, 0.015 and 1.2, for a wide range of pressure ratios and they have computed for each case the mass flow rate, the momentum flux, and the specific impulse. It has been deduced that the thick orifice has a higher propulsion efficiency.

In the present work, we apply the DSMC method to investigate numerically the flow of a monatomic gas into vacuum through circular tubes with length to radius ratios ranging from 0 up to 10. Numerical results for the mass flow rates and the macroscopic distributions of the flow (velocity, pressure, and temperature) are presented in the whole range of the Knudsen number. In addition, we study the effect of

a)Electronic mail: diva@mie.uth.gr

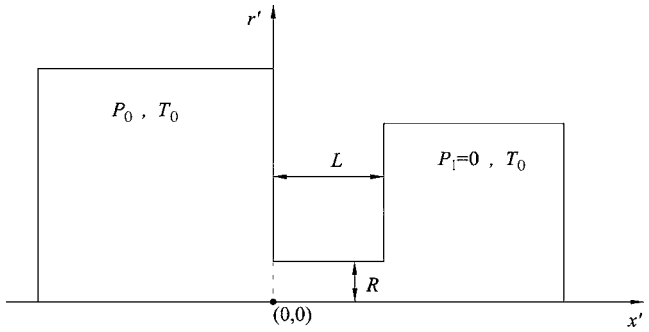


FIG. 1. Short tube geometry.

the gas-surface interaction model by introducing the Cercignani-Lampis scattering kernel[14] as well as the effect of the intermolecular potential model by using the hard sphere and the variable hard sphere models. For specific flow configurations, the numerical results are compared successfully with the corresponding results from previous experimental[15,16] and computational[11] works.

## II. STATEMENT OF THE PROBLEM AND DEFINITIONS

Consider a tube of radius $R$ and finite length $L$ connecting two semi-infinite reservoirs. The geometric configuration with the coordinate system $(x',r')$ and its origin are shown in Fig. 1. A monotomic gas in the left reservoir is maintained at equilibrium pressure $P_0$ and temperature $T_0$, while in the right container, the pressure $P_1$ is kept so low that it is assumed to be equal to zero $(P_1=0)$.

Two parameters determine the solution of this flow configuration. The first one is a geometric parameter, namely, the length to radius ratio $L/R$ of the tube. The second one is the rarefaction parameter $\delta$, defined as[1]

$$\delta = \frac{RP_0}{\mu_0 v_0}. \tag{1}$$

Here, the radius $R$ of the tube is taken as the characteristic macroscopic length, $P_0$ is the reference pressure, $\mu_0$ is the gas viscosity at reference temperature $T_0$, and $v_0=\sqrt{2kT_0/m}$ is the most probable molecular speed with $k$ denoting the Boltzmann constant and $m$ the molecular mass of the gas. It is also noted that the rarefaction parameter $\delta$ is proportional to the inverse Knudsen number.

Our objective is to find the mass flow rate through the tube and the detailed flow field in the tube and in the two reservoirs in terms of the parameters $L/R$ and $\delta$. The results will be presented in terms of the reduced flow rate defined as

$$W = \frac{\dot{M}}{\dot{M}_0}, \tag{2}$$

where $\dot{M}_0$ is the flow rate through an orifice $(L/R=0)$ at the free-molecular limit $(\delta=0)$. The quantity $\dot{M}_0$ can be easily computed in an analytical manner to yield

$$\dot{M}_0 = \frac{\sqrt{\pi}R^2}{v_0} P_0. \tag{3}$$

Also, the dimensionless macroscopic distributions of velocity $[u_x(x,r),u_r(x,r)]$, density $n(x,r)$, pressure $P(x,r)$, and temperature $T(x,r)$ are defined by dividing the dimensional ones with the corresponding characteristic quantities $v_0$, $n_0$, $P_0$, and $T_0$ respectively, with $P_0=n_0kT_0$. The quantities $r=r'/R$ and $x=x'/R$ are the dimensionless radial and axial coordinates. All results in Sec. IV are presented in terms of dimensionless quantities.

## III. SPECIFIC ISSUES OF THE IMPLEMENTED DSMC SOLUTION

Recently, the DSMC algorithm based on the Non Time Counter (NTC) scheme[8] has been developed and applied successfully to the simulation of rarefied gas flow through an orifice $(L/R=0)$.[17] In the present work, this code is accordingly extended to that of simulating rarefied gas flow through a short tube, i.e., for arbitrary values of the ratio $L/R$. Since the details of the algorithm are well described and thoroughly explained in previous works,[8,17] its detailed description is omitted and only the specific issues related to the present formulation are provided for completeness and clarity.

The axisymmetric computational domain is shown in Fig. 2. It is consisting of the tube defined by $(0\leqslant r\leqslant 1, 0\leqslant x$

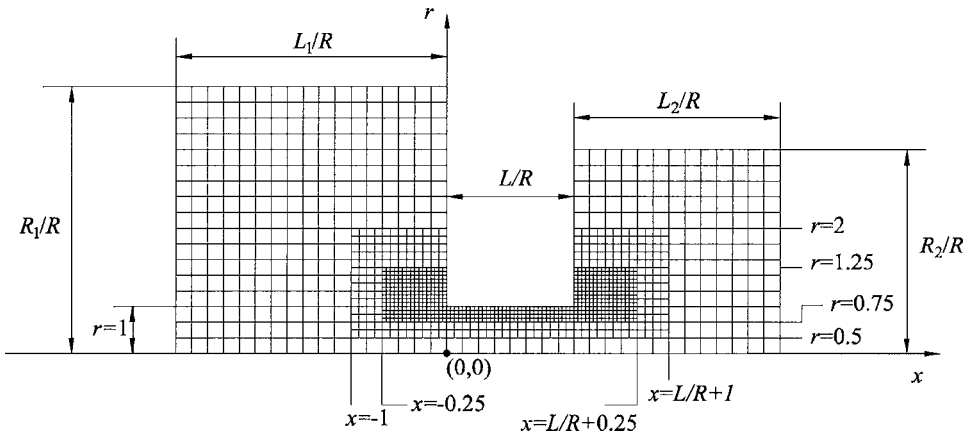


FIG. 2. Computational domain with nonuniform grid.

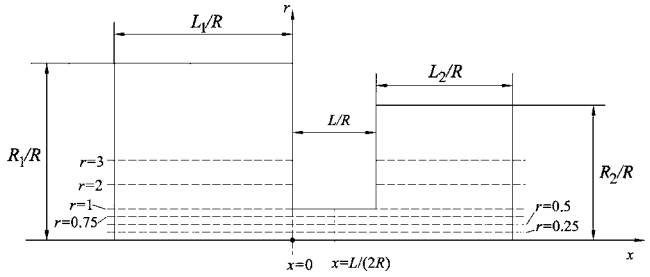


FIG. 3. Weighting zones.

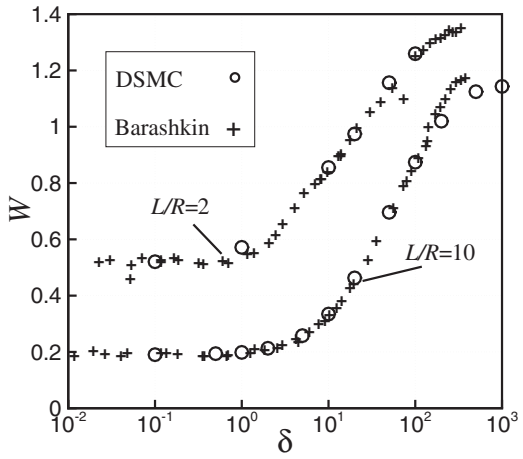


FIG. 4. Comparison between the present numerical results and the corresponding experimental ones by Barashkin (Ref. 15).

$\leqslant L/R$) and two large cylinders defined by $(0\leqslant r\leqslant R_1/R, -L_1/R\leqslant x\leqslant 0)$ and $(0\leqslant r\leqslant R_2/R, L/R\leqslant x\leqslant (L+L_2)/R)$, which correspond to the computational volumes of the upstream and downstream reservoirs, respectively. Several computational sizes of the two reservoirs have been tested and the minimum ones which guarantee invariance in the results less than 1% were selected, namely, $L_1=R_1=8R$ and $L_2=R_2=4R$. The computational grid is structured and nonuniform containing cells with three different sizes. These three different areas of the grid are shown in Fig. 2. Such a three level grid is required in order to capture the steep macroscopic gradients close to the boundaries and maintain reasonable computational efficiency.

In order to maintain, as much as possible, uniform distributions of particles at each cell in the whole computational domain, the concept of the weighting factor has been introduced. In addition to the radial weighting zones introduced in Ref. 17, a number of axial weighting zones have been added. More specifically, in all cases, seven radial and three axial weighting zones have been applied. The decomposition of the computational domain into weighting zones is presented in Fig. 3. Particles which are moving toward the axis $r=0$ or from left to right and enter a new radial or axial weighting zone, respectively, are doubled with prescribed weights equal to one-half of the weight of the initial particles. On the other hand, when particles are moving away from the axis $r=0$ or from right to left and enter a new weighting zone, half of them are completely eliminated, while the other half is maintained with prescribed weights equal to the double weight of the initial particles. By following this practice, the statistical scattering of the results is significantly reduced, while the same number of model particles is maintained. The number of modeled particles and of computational cells used in the simulations strongly depends on the ratio of the length over the radius of the tube $(L/R)$. The total number of particles and cells varies from $2\times 10^7$ to $3\times 10^7$ and from $4\times 10^4$ and $8\times 10^4$, respectively, depending on the ratio $L/R$.

Initially, the modeled particles are distributed uniformly in the left container with the Maxwellian distribution corresponding to the equilibrium state far from the tube inlet. Then, the simulation starts by advancing in small time steps $\Delta t$, such that $\Delta t<t_m$, where $t_m$ is the mean collision time. Following the standard procedure at each time step, the dy-

TABLE I. Dimensionless flow rate $W$ vs $L/R$ and $\delta$ for the HS model and diffuse gas-surface interaction.

| | $W$ | | | | | |
|---|---|---|---|---|---|---|
| $\delta$ | $L/R=0$ | $L/R=0.1$ | $L/R=0.5$ | $L/R=1$ | $L/R=5$ | $L/R=10$ |
| 0.0 | 1.000 | 0.953 | 0.801 | 0.672 | 0.311 | 0.192 |
| 0.1 | 1.014 | 0.965 | 0.812 | 0.680 | 0.312 | 0.190 |
| 0.5 | 1.069 | 1.018 | 0.855 | 0.715 | 0.322 | 0.194 |
| 1 | 1.129 | 1.074 | 0.902 | 0.754 | 0.334 | 0.198 |
| 2 | 1.221 | 1.165 | 0.981 | 0.819 | 0.361 | 0.213 |
| 5 | 1.374 | 1.312 | 1.117 | 0.948 | 0.436 | 0.258 |
| 10 | 1.463 | 1.404 | 1.220 | 1.062 | 0.543 | 0.335 |
| 20 | 1.512 | 1.462 | 1.302 | 1.168 | 0.695 | 0.463 |
| 50 | 1.534 | 1.498 | 1.383 | 1.287 | 0.917 | 0.696 |
| 100 | 1.533 | 1.508 | 1.435 | 1.358 | 1.068 | 0.874 |
| 200 | 1.529 | 1.512 | 1.462 | 1.412 | 1.184 | 1.020 |
| 500 | 1.526 | 1.515 | 1.484 | 1.449 | 1.271 | 1.125 |
| 1000 | 1.523 | 1.515 | 1.494 | 1.456 | 1.282 | 1.143 |
| 2000 | 1.522 | 1.517 | 1.493 | 1.458 | 1.284 | 1.145 |

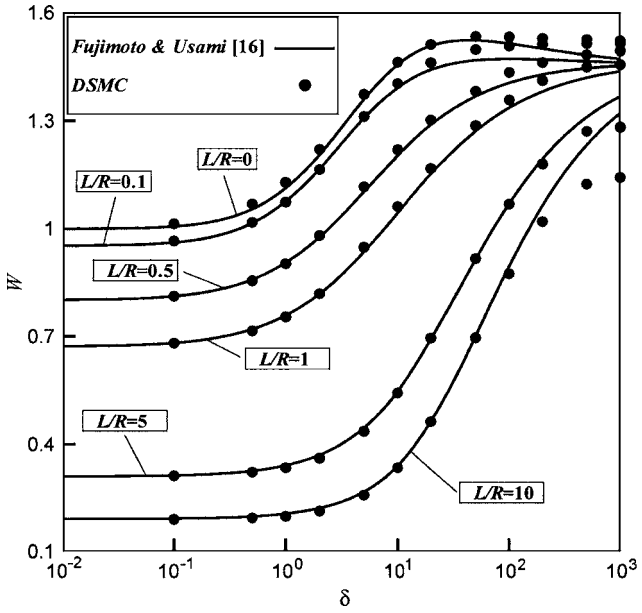


FIG. 5. Comparison between the present numerical results and the corresponding ones by Fujimoto and Usami (Ref. 16), based on their approximate formula (21).

namic motion of the particles is split into the free motion of the particles (first stage) followed by their collisions (second stage).

During the first stage, all of the particles are freely moved through some distance defined by their molecular velocities and the time step. During this free motion, some of them may interact with the solid boundaries of the tube or of the reservoirs. The interaction of particles with solid boundaries is simulated by diffuse reflection. To investigate the influence of the nondiffuse scattering, the Cercignani-Lampis model[2,14] was used for some values of the gas rarefaction and length to radius ratio. The Cercignani-Lampis model has two accommodation coefficients (one for the tangential momentum and one for the kinetic energy due to the molecular velocity normal to the surface) and provides a more physical description of the gas scattering on solid surfaces. Since gas-surface interaction plays an important role in the present flow configuration, results for both purely diffuse and partially diffuse-specular reflections have been provided. Also during this free motion, some particles may get out from the computational domain. These particles are completely eliminated from the rest of the simulation. At the same time, new particles are generated at the boundaries of the upstream reservoir having the corresponding Maxwellian distributions. The number of particles entering the flow is defined by

$$N_b = \frac{1}{4} A n_0 v_t \Delta t, \tag{4}$$

where $A$ is the area of the boundary, $n_0$ is the equilibrium numerical density, and $v_t$ is the corresponding mean thermal speed. Upon establishing steady state conditions, the number of particles leaving and entering the computational domain is approximately the same and therefore the total number of simulated particles remains practically constant.

TABLE II. Dimensionless flow rate $W$ for various boundary conditions and intermolecular potentials: Diffuse ($\alpha_n=\alpha_t=1$); CL, Cercignani-Lampis ($\alpha_n=1, \alpha_t=0.5$); HS, hard spheres; VHS, variable hard spheres (helium, $\omega=0.66$).

| | | $W$ | | |
|---|---|---|---|---|
| | | HS | | VHS |
| $L/R$ | $\delta$ | Diffuse | CL | diffuse |
| 0 | 0.1 | 1.014 | 1.010 | 1.014 |
| | 1 | 1.129 | 1.129 | 1.115 |
| | 10 | 1.462 | 1.454 | 1.446 |
| | 100 | 1.534 | 1.523 | 1.531 |
| | 1000 | 1.523 | 1.516 | 1.522 |
| 0.1 | 0.1 | 0.965 | 0.983 | 0.963 |
| | 1 | 1.074 | 1.093 | 1.063 |
| | 10 | 1.404 | 1.415 | 1.388 |
| | 100 | 1.508 | 1.507 | 1.507 |
| | 1000 | 1.515 | 1.509 | 1.514 |
| 1 | 0.1 | 0.680 | 0.802 | 0.680 |
| | 1 | 0.754 | 0.891 | 0.746 |
| | 10 | 1.062 | 1.183 | 1.041 |
| | 100 | 1.358 | 1.396 | 1.349 |
| | 1000 | 1.456 | 1.466 | 1.456 |
| 10 | 0.1 | 0.190 | 0.343 | 0.190 |
| | 1 | 0.198 | 0.363 | 0.197 |
| | 10 | 0.335 | 0.493 | 0.318 |
| | 100 | 0.874 | 0.932 | 0.842 |
| | 1000 | 1.143 | 1.162 | 1.117 |

During the second stage, the intermolecular interactions at each cell is simulated as in Ref. 17. The intermolecular potential was modeled using the hard-sphere (HS) and the variable hard sphere (VHS) models.[8] In the former case, the total cross section is constant, the viscosity is proportional to $\sqrt{T}$, and the deduced dimensionless results are general since they can be presented in terms of $\delta$, i.e., it is not necessary to prescribe a specific gas. In the latter case, the total cross section is a function of the relative velocity between two collided particles and the viscosity is proportional to $T^{\omega}$, where the parameter $\omega$ characterizes a specific gas. In the next section, we study the effect of the intermolecular potential by comparing the corresponding results between the HS model and the VHS model for helium ($\omega=0.66$).

The dynamic motion of the particles is simulated for a sufficient number of time steps such that steady-state flow conditions in the computational domain are established. The dimensionless time step is always $\Delta t/t_m=0.01\delta$ and in all cases we consider that steady-state conditions have been obtained when the statistical scattering of the dimensionless flow rate $W$ is less than 1%. To estimate $W$, the difference between the particles crossing the inlet cross section of the tube at $x=0$ from left to right and from right to left denoted by $N^+$ and $N^-$, respectively, is computed. Upon convergence, this quantity $(N^+-N^-)$ is equal to the corresponding one at

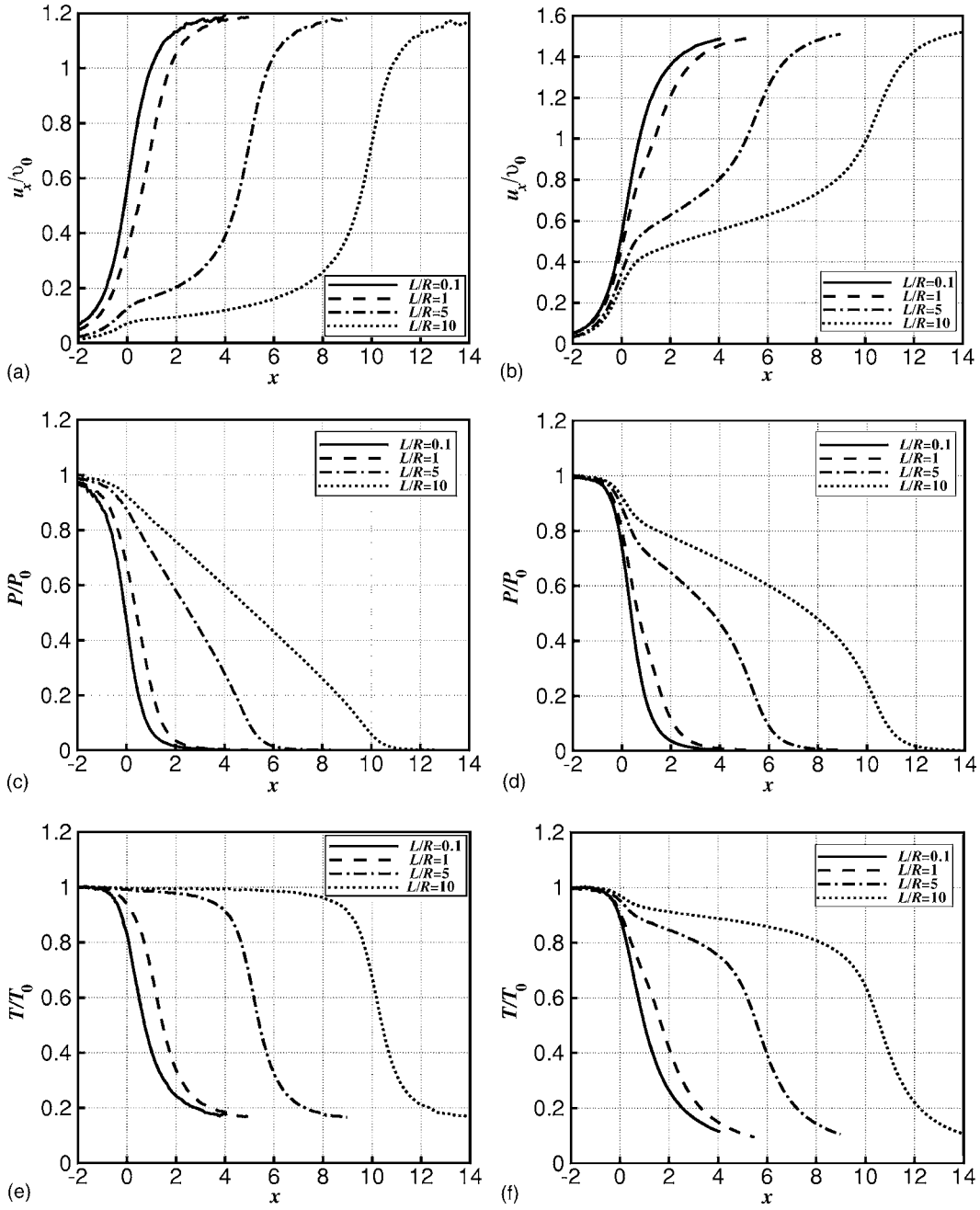


FIG. 6. Dimensionless axial velocity (top), pressure (middle), and temperature (bottom) distributions along $r=0$ for $\delta=1$ (left) and $\delta=100$ (right) and various $L/R$.

the exit cross section of the tube at $x=L/R$. It is pointed that as the length to radius ratio is increased, the required number of time steps is also increased. This is easily justified since the relative scattering of the flow is of the order $\sqrt{N^+}/(N^+ - N^-)$ and as $L/R$ is increased, then $N^-$ is increased as well. Also, as the rarefaction parameter $\delta$ is increased and we are approaching the continuum limit, the overall computational effort is significantly increased because the number of the intermolecular collision to be simulated is large.

## IV. RESULTS AND DISCUSSIONS

Calculations have been carried out in the wide range of the rarefaction parameter $\delta$ from 0 to 2000 and for $L/R=0$, 0.1, 0.5, 1, 2, 5, and 10. The results presented in this section include, for all these cases, the dimensionless flow rate $W$ as well as contours and profiles of macroscopic distributions with practical interest.

### A. Dimensionless flow rate

Results for the dimensionless flow rate $W$ for the purely diffuse boundary conditions and the HS model are presented in the Table I in terms of $\delta$ and $L/R$. The purely diffuse reflection can be easily deduced from the Cercignani-Lampis model by setting both the tangential momentum coefficient $a_t$ and the kinetic energy coefficient $a_n$ equal to 1. The case

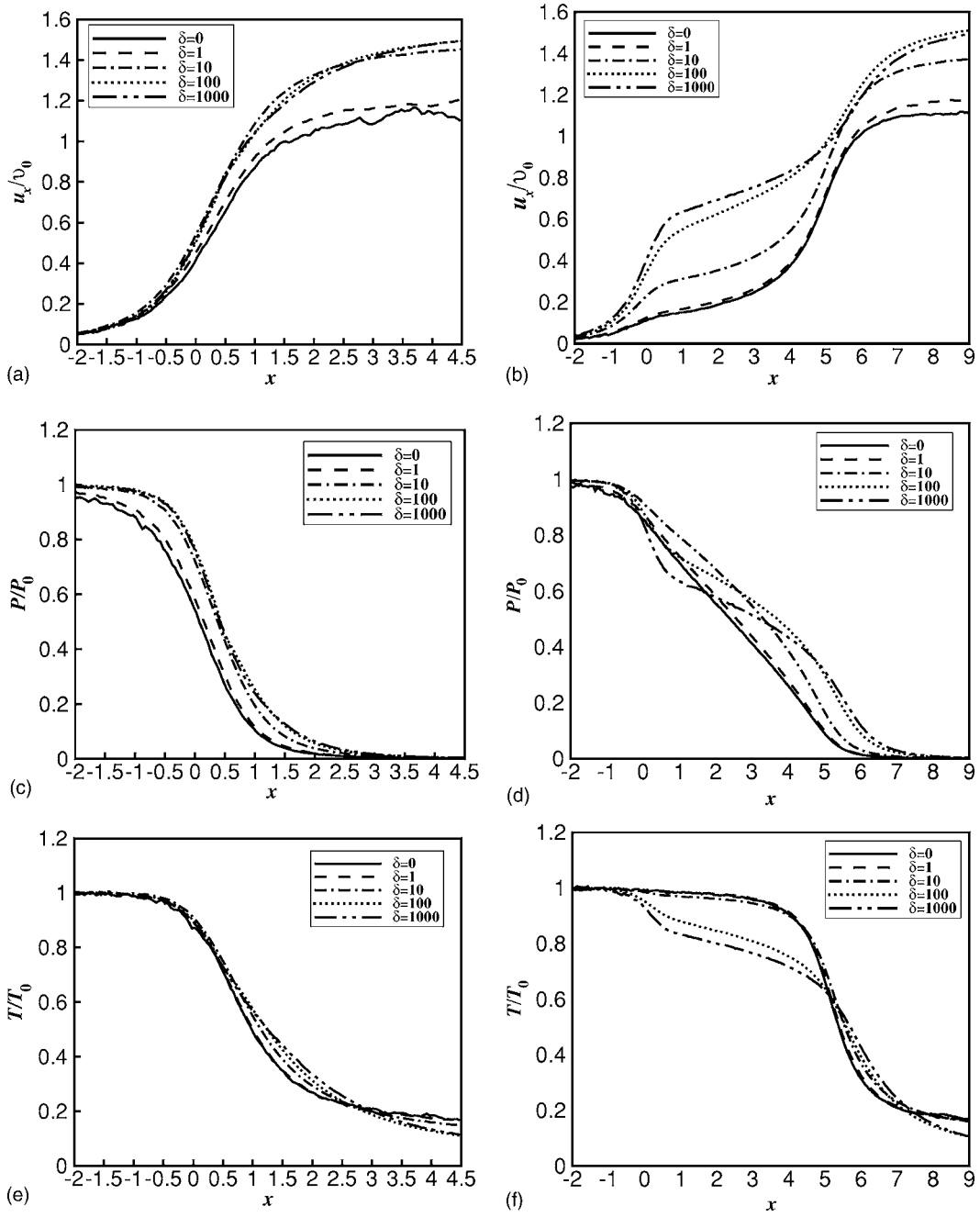


FIG. 7. Dimensionless axial velocity (top), pressure (middle), and temperature (bottom) distributions along $r=0$ for $L/R=0.5$ (left) and $L/R=5$ (right) and various $\delta$.

of $L/R=0$, which corresponds to flow through an orifice, has been included for completeness and comparison purposes. As expected, the results of the present work for this specific case are identical with the corresponding ones in Ref. 17. In addition, the results corresponding to the free-molecular regime ($\delta=0$) coincide, within the computational error, with those obtained in Ref. 1 by the test particle method (fifth column of Table 30 in Ref. 1).

By analyzing the results of $W$ in terms of $\delta$ and $L/R$, the following remarks can be deduced. For fixed values of $\delta$, it can be seen that $W$ decreases by increasing the length $L/R$. It is noted that at $\delta=1$, the values of $W$ between $L/R=0.1$ and 10 are reduced more than five times, while at $\delta=10^2$, the corresponding reduction is less than two times. For fixed length $L/R$, $W$ is increased as $\delta$ is increased from the free-molecular limit ($\delta=0$) up to the hydrodynamic one ($\delta=2000$). The dependency of $W$ on $\delta$ for all $L/R$ can be clearly distinguished in three regions. More specifically, as $\delta$ is increased, at small $\delta$, the reduced flow rate $W$ is increased very slowly. At intermediate $\delta$, there is a significant increase of $W$, which is approximately linearly proportional to log $\delta$. Finally, at large values of $\delta$, $W$ keeps increasing very weakly, reaching asymptotically the continuum results at the hydro-

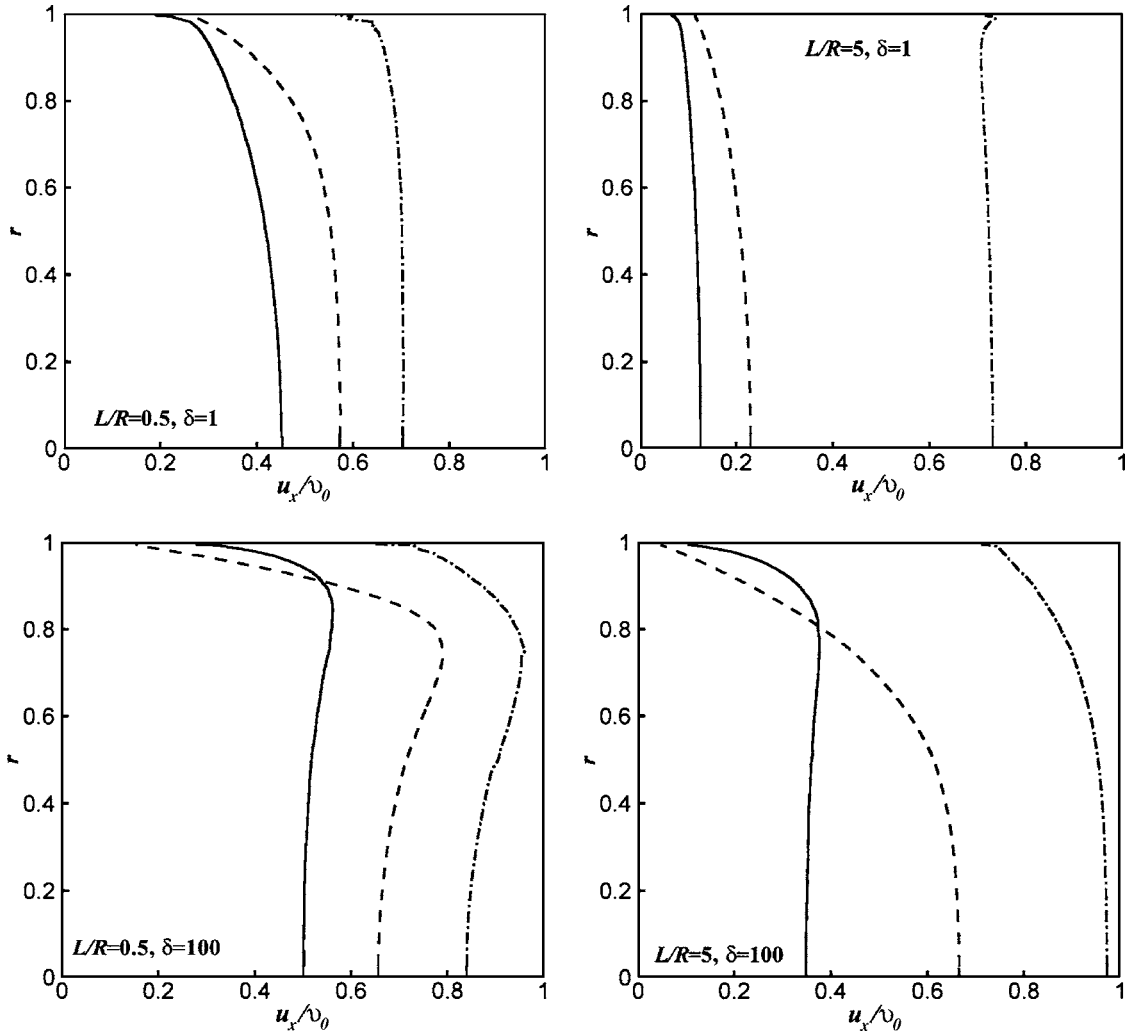


FIG. 8. Dimensionless axial velocity profiles at the inlet ($x=0$, —), middle ($x=L/(2R)$, - - -), and outlet ($x=L/R$, -·-·-) of the tube for characteristic combinations of $L/R$ and $\delta$.

dynamic limit ($\delta\to\infty$). The exact values of $\delta$, determining the limits of each of the three regions, depend on $L/R$ and can be estimated from Table I.

At this point a comparison with experimental results available in the literature is provided. In Fig. 4, numerical results of the present work for the dimensionless flow rate $W$ for $L/R=2$ and 10 are compared with the corresponding experimental results by Barashkin[15] for $L/R=1.92$ and 10.66, respectively. It is seen that although the experimental results are for the polyatomic gas of $CO_2$, while the numerical ones are for a monotomic gas, the agreement in both cases is excellent for all $\delta$. Any discrepancies are within the experimental uncertainties. Fujimoto and Usami,[16] based on their experimental results, have proposed an approximate formula [Eq. (21) in Ref. 16], supplemented by a specific procedure to obtain approximate results for the dimensionless flow rate $W$. In Fig. 5, the numerical results of the present work are compared with the corresponding experimental ones produced according to Ref. 16. It is seen that the agreement is very good for all $L/R$ and for $\delta<500$.

Finally, a comparison with the very recent computational results of Lilly *et al.*[10] has been performed. We examine both length to radius ratios that they have considered ($L/R=0.03$ and 2.4), with upstream pressures $P_1=1071$ and 410 Pa, which correspond to reference rarefaction parameters $\delta=24.7$ and 9.45, respectively. In all cases, the discrepancy between the present numerical results and the ones in Ref. 10 are less than 2%. This agreement provides some additional confidence to the accuracy of our solutions in the whole range of $L/R$ examined in the present work.

### B. Gas-surface interaction

In Table II, the dimensionless flow rate $W$ is shown for specific values of $L/R$ and $\delta$ using the diffuse (third column) and Cercignani-Lampis (fourth column) boundary conditions. In the latter one, the accommodation coefficients are taken to be $\alpha_t=0.5$ and $\alpha_n=1$. The case $L/R=0$ is also included for comparison. The HS model has been used.

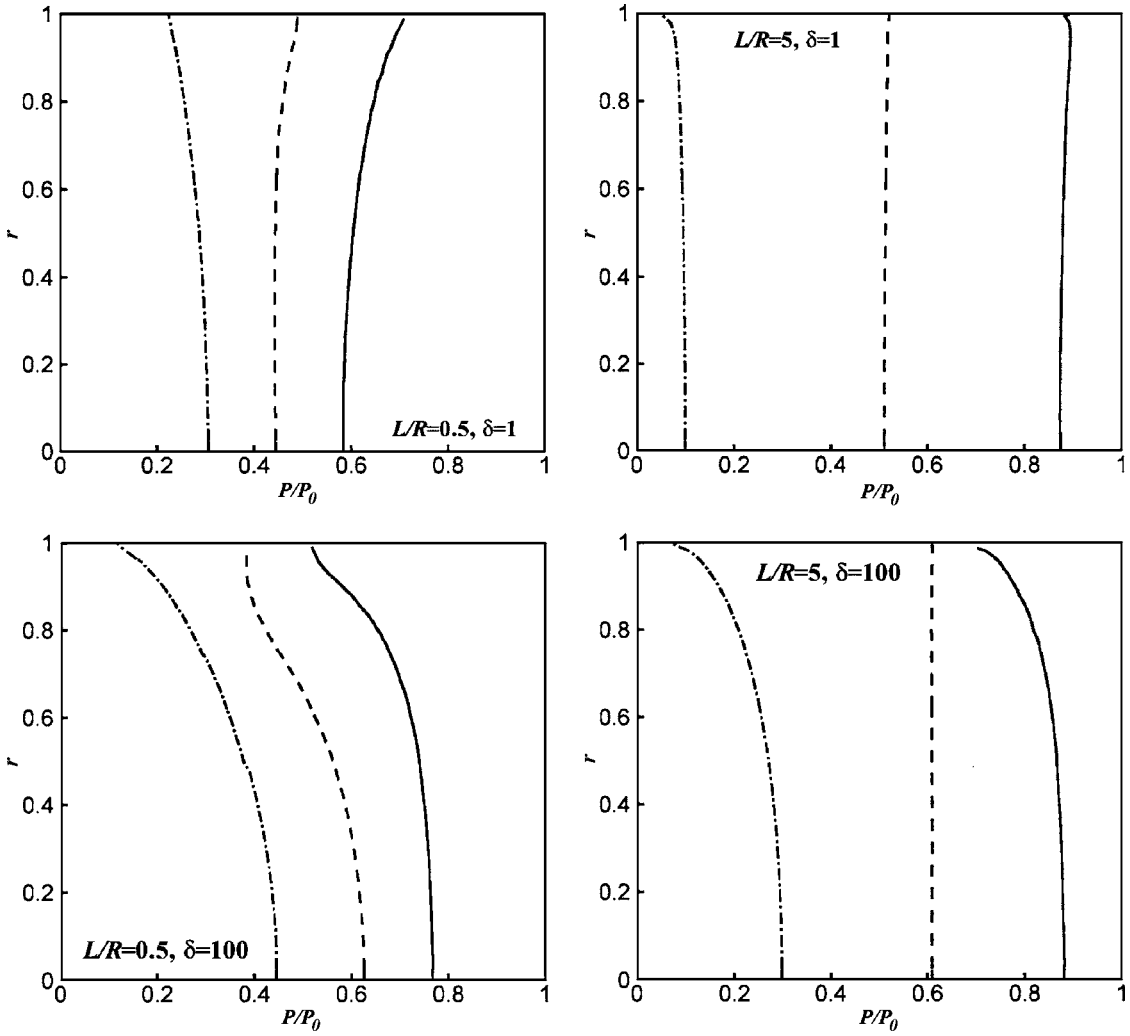


FIG. 9. Dimensionless pressure profiles at the inlet ($x=0$, —), middle ($x=L/(2R)$, - - -), and outlet ($x=L/R$, ·---·) of the tube for characteristic combinations of $L/R$ and $\delta$.

It is clearly seen that as the ratio $L/R$ is increased, the effect of the gas-surface interaction law is drastically increased. Specifically, for $L/R=0.1$, 1, and 10 and for the same $\delta=1$, the estimates of $W$ in the fourth column of Table II compared to the corresponding ones in the third column are increased by 1.8%, 18.4%, and 83.3%, respectively. The same tendency is observed for all values of $\delta$. Therefore, the dependency of the flow rate on the type of gas-surface interaction is weak for $L/R<1$ but it becomes strong for $L/R \geqslant 1$.

It is also seen from Table II that the effect of the gas-surface interaction has a weak dependency on $\delta$. In particular, for $\delta=0.1$, 1, and 10 and for the same $L/R=1$, the estimates of $W$ in the fourth column Table II are increased by 17.9%, 18.2%, and 11.4%, respectively, compared to the corresponding ones in the third column. In general, as $\delta$ is increased, the dependency on the gas-surface interaction is significantly decreased and it is computationally negligible in the slip and continuum regimes.

### C. Intermolecular potential

As mentioned above, the influence of the intermolecular potential on the flow characteristics is studied by implementing in addition to the HS, the VHS model. In the last column of Table II, the dimensionless flow rate $W$ obtained for the VHS model corresponding to helium and assuming the diffuse boundary conditions is tabulated. By comparing the estimates of $W$ between the third and fifth columns of Table II, it may be deduced that the sensitivity of $W$ on the intermolecular potential is very weak. Actually, for $L/R \leqslant 1$ the results are in most cases identical and if in some cases there are differences, they are within the numerical error ($\leqslant 1\%$). For $L/R=10$ and large $\delta$, there is some influence of the intermolecular potential on $W$ but it is small and the maximum variation is 5.3%. It can be concluded that for all values of $L/R$ and $\delta$ examined, the dependency of the results on the model describing the intermolecular potential is insignificant.

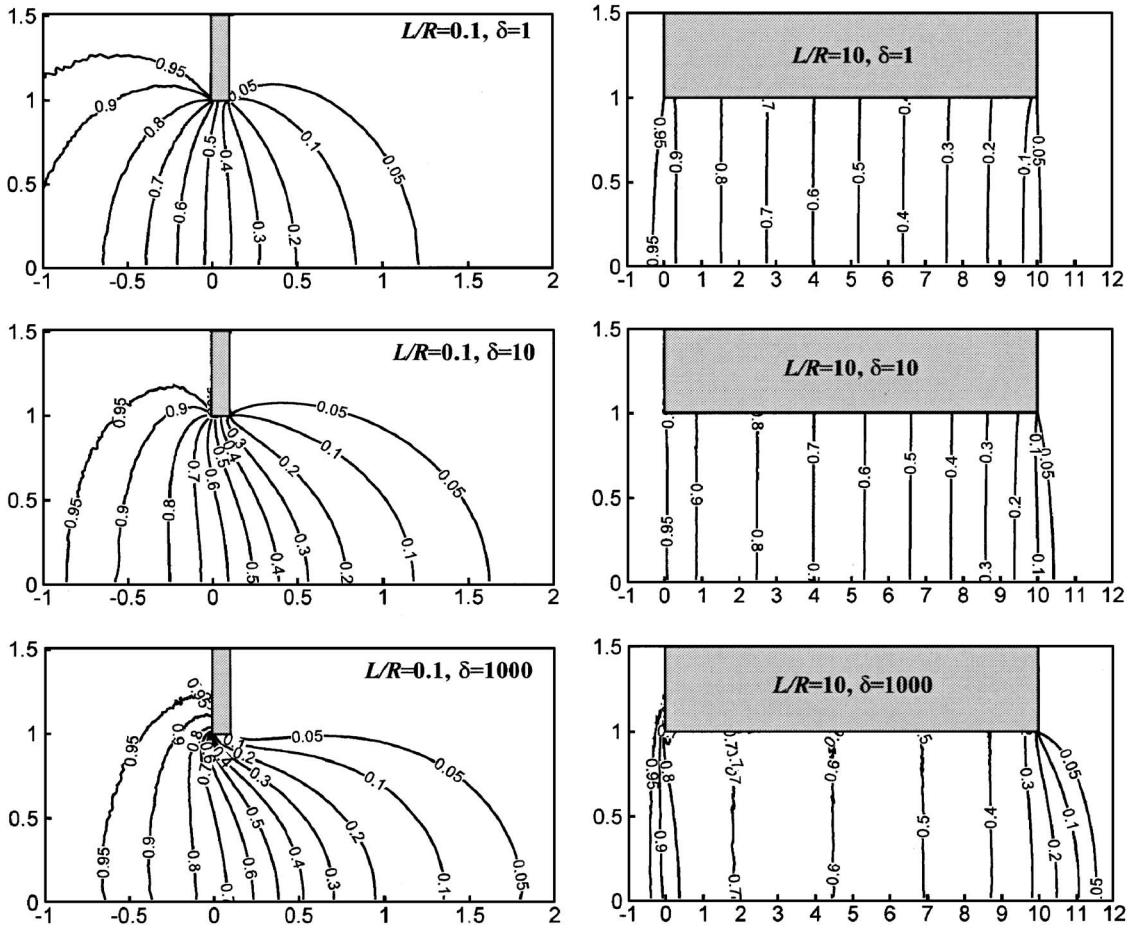


FIG. 10. Dimensionless pressure isolines in the region around and inside the tube for $L/R=0.1$ and 10 and $\delta=1$ (top), 10 (middle), and 1000 (bottom).

### D. Flow field

The distributions of the dimensionless axial velocity, pressure, and temperature along the symmetry axis $r=0$ and $-2 \leqslant x \leqslant L/R+4$ are shown in Fig. 6 for $\delta=1$ and $10^2$ and various values of $L/R$. In all cases, as $x$ is increased, the axial velocity is increased, while the pressure and the temperature are decreased. It is seen that the velocity is rapidly increased just before the inlet and after the outlet of the tube, while inside the tube it is also increased but with a smaller pace. This behavior is more clearly demonstrated at $L/R=5$ and 10. The maximum value of the axial velocity along the symmetry axis occurs far downstream and it is independent of the ratio $L/R$. However, it depends on $\delta$ and it is significantly higher for $\delta=10^2$ compared to the one for $\delta=1$. As expected, the pressure and temperature distributions qualitatively have the inverse behavior compared to the axial velocities.

The effect of the rarefaction parameter $\delta$ on the same quantities as above is shown in detail in Fig. 7 by plotting these distributions for $L/R=0.5$ and 5 and for various values of $\delta$. It is seen that the results for $\delta \leqslant 1$ and for $\delta \geqslant 10^2$ are very close to the corresponding ones at the free-molecular limit ($\delta=0$) and at the continuum limit ($\delta=2000$), respectively. This is in agreement with the tabulated dimensionless flow rates in Table I, where, as it has been pointed out, $W$ remains almost the same at small and large $\delta$ and it is significantly increased in the range $1<\delta<10^2$. It is interesting to note that for large $\delta$, the rapid increase in the velocity before and after the tube is about the same, while in the case of small $\delta$, the increase in the velocity at the outlet of the tube is significantly higher than the one at the inlet of the tube. This is clearly demonstrated at $L/R=5$. Again, the behavior of the pressure and temperature distributions is inversely proportional to the one of the velocity.

Profiles of the dimensionless axial velocity at the inlet ($x=0$), middle ($x=L/(2R)$), and outlet ($x=L/R$) of the tube are shown in Fig. 8 for various values of $L/R$ and $\delta$. The corresponding pressure profiles are shown in Fig. 9. The combinations $L/R=0.5$, $\delta=1$ and $L/R=5$, $\delta=10^2$ may be considered as indicative for the cases when both $L/R$ and $\delta$ are small and large, respectively, while the other two, i.e., $L/R=0.5$, $\delta=10^2$ and $L/R=5$, $\delta=1$, are representative for the cases when one of the two parameters is small and the other is large. For each of the four cases, the presented profiles are characteristic for the flow evolution (velocity acceleration and pressure drop of the gas) along the tube.

We close our discussion by presenting a more complete picture of the flow field in Figs. 10 and 11, where isolines of the dimensionless pressure and Mach number are plotted in the region around and inside the tube for $L/R=0.1$ and 10 and $\delta=1$, 10, and 1000. Based on these results, it is obvious

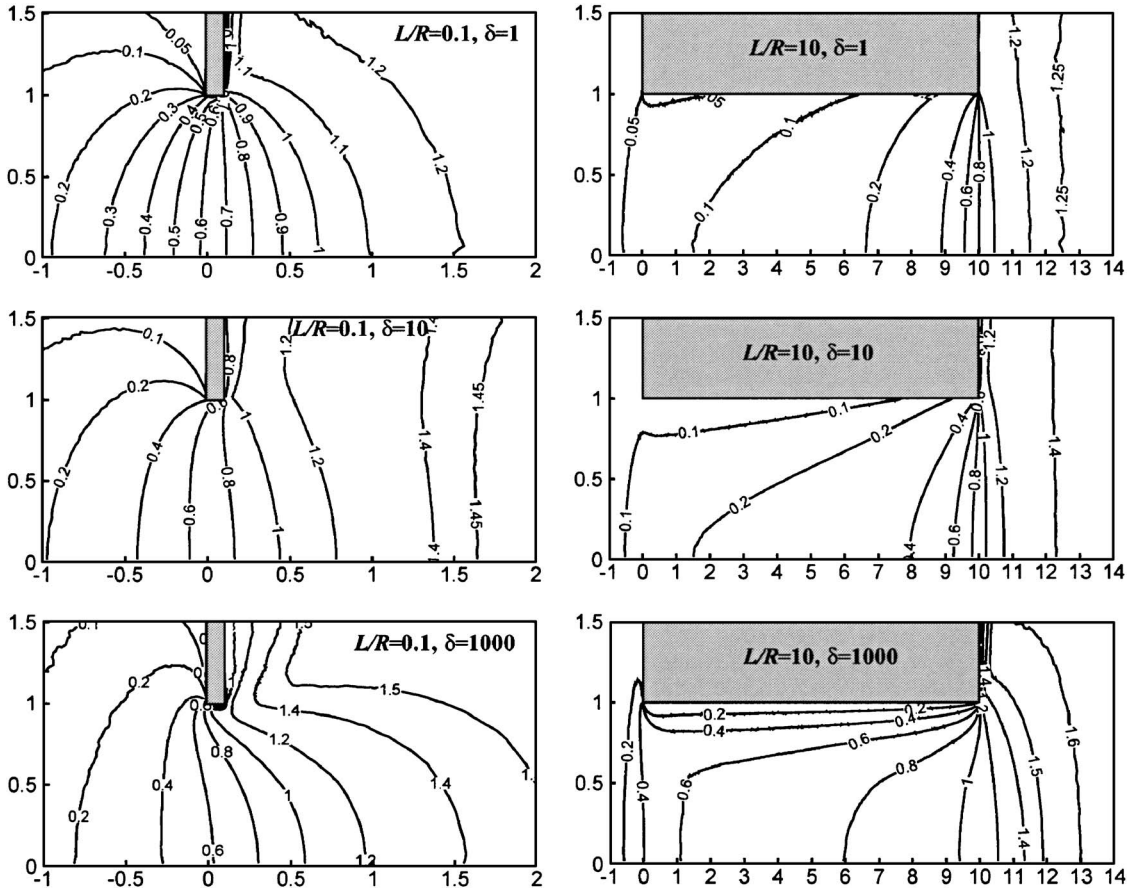


FIG. 11. Isolines of local Mach number in the region around and inside the tube for $L/R=0.1$ (left) and 10 (right) and $\delta=1$ (top), 10 (middle), and 1000 (bottom).

that when $\delta$ is kept constant and $L/R$ is changed from 0.1 to 10, the flow field is significantly modified both qualitatively and quantitatively. In addition, when $L/R$ is kept constant and $\delta$ is changed from 1 to 10 and then to 1000, the magnitude of the macroscopic quantities is altered, while the qualitative characteristics of the flow field remain the same.

## V. CONCLUDING REMARKS

The DSMC method has been applied to study the rarefied gas flow into vacuum through a short tube. The gas-surface interaction is simulated by using both the diffuse and the Cercignani-Lampis scattering kernels. The intermolecular potentials are estimated using the HS and the VHS models. The nonequilibrium effects at the inlet and outlet of the tube have been considered by including in the computational domain large volumes of the upstream and downstream reservoirs. Dimensionless results for the flow rate and the macroscopic distributions of the flow (velocity, pressure, and temperature) are presented in the whole range of gas rarefaction ($0\leqslant\delta\leqslant 2\times 10^3$) and for various length to radius ratios ($0\leqslant L/R\leqslant 10$). For specific flow configurations, the numerical results are found to be in very good agreement with available experimental results. It is deduced that modifying the parameters $L/R$ as well as $\delta$ has a significant impact on the magnitude of the flow quantities. However, the qualitative characteristics of the flow field alter significantly only when the length of the tube is changed, while they remain almost insensitive when the rarefaction parameter is changed. In addition, the dependency of the results on the gas-surface interaction law is significant only for $L/R\geqslant 1$, while their dependency on the intermolecular potential model is, in general, modest.

## ACKNOWLEDGMENTS

Partial support of this work by the Association Euratom-Hellenic Republic and by the Conselho Nacional de Desenvolvimento Cientifico e Tecnologico (CNPq, Brazil) is gratefully acknowledged.

[1]F. Sharipov and V. Seleznev, J. Phys. Chem. Ref. Data **27**, 657 (1998).
[2]C. Cercignani, *The Boltzmann Equation and its Application* (Springer, New York, 1988).
[3]D. Valougeorgis and J. R. Thomas, Phys. Fluids **29**, 423 (1986).
[4]F. Sharipov, J. Vac. Sci. Technol. A **14**, 2627 (1996).
[5]F. Sharipov, J. Vac. Sci. Technol. A **17**, 3062 (1999).
[6]F. Sharipov, Eur. J. Mech. B/Fluids **22**, 145 (2003).
[7]S. Naris, D. Valougeorgis, D. Kalempa, and F. Sharipov, Phys. Fluids **17**, 100607 (2005).
[8]G. A. Bird, *Molecular Gas Dynamics and the Direct Simulation of Gas Flows* (Oxford University Press, Oxford, 1994).

[9]H. Shinagawa, H. Setyawan, T. Asai, Y. Yuuichi, and K. Okuyama, Chem. Eng. Sci. **57**, 4027 (2002).
[10]T. C. Lilly, N. P. Selden, S. F. Gimelshein, A. D. Ketsdever, and G. N. Markelov, AIAA Paper 2004–2385 (2004).
[11]T. C. Lilly, S. F. Gimelshein, A. D. Ketsdever, and G. N. Markelov, Phys. Fluids **18**, 093601 (2006).
[12]M. Usami and K. Teshima, JSME Int. J., Ser. B **42**, 369 (1999).
[13]R. Hanks and H. Weissberg, J. Appl. Phys. **35**, 142 (1964).
[14]C. Cercignani and M. Lampis, Transp. Theory Stat. Phys. **1**, 101 (1971).
[15]S. T. Barashkin, "Experimental investigation of flows of gas into vacuum," Ph.D. thesis, Ural State Technical University (1977).
[16]T. Fujimoto and M. Usami, J. Fluids Eng. **106**, 367 (1984).
[17]F. Sharipov, J. Fluid Mech. **518**, 35 (2004).